Microporous and Mesoporous Materials 373 (2024) 113119

Contents lists available at ScienceDirect

Microporous and Mesoporous Materials

journal homepage: www.elsevier.com/locate/micromeso

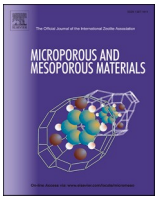

Systematic study of the implications of calcination and solvent extraction of the surfactant in MCM-41-type mesoporous silica nanoparticles

Vicente Candela-Noguera [a,c,d,**], Pedro Amorós [b], Elena Aznar [a,c,d,e], María Dolores Marcos [a,c,d,e,*], Ramón Martínez-Máñez [a,c,d,e,***]

[a] Instituto Interuniversitario de Investigación de Reconocimiento Molecular y Desarrollo Tecnológico (IDM), Universitat Politècnica de València, Universitat de València, Camino de Vera s/n, 46022, Valencia, Spain
[b] Instituto Universitario de Ciencia de los Materiales (ICMUV), Universitat de València, Catedrático José Beltrán 2, 46980, Paterna, Valencia, Spain
[c] CIBER de Bioingeniería, Biomateriales y Nanomedicina, Instituto de Salud Carlos III, Spain
[d] Unidad Mixta UPV-CIPF de Investigación en Mecanismos de Enfermedades y Nanomedicina, Universitat Politècnica de València, Centro de Investigación Príncipe Felipe, Valencia, Spain
[e] Unidad Mixta de Investigación en Nanomedicina y Sensores, Universitat Politècnica de València, IIS La Fe, Valencia, Spain

ARTICLE INFO

Keywords:
Mesoporous silica nanoparticles
Surfactant removal
Efficiency
Condensation degree
Porosity
Biocompatibility
Biodegradability

ABSTRACT

Mesoporous silica nanoparticles (MSN) have been growing in recent years in a broad range of applications, such as nanomedicine, catalysis, and gas storage. For the preparation of MSN, especially in nanomedicine applications, the extraction of the surfactant template, generally 1-hexadecyltrimethylammonium bromide (CTAB), is required. Several methods to remove the surfactant from MNS have been reported in the literature, such as calcination, solvent extraction, and dialysis. Depending on the method employed, the materials obtained have different properties; however, a systematic study that compares the use of different surfactant extraction methods and their implications in the final characteristics of the MSN has not been reported. Hence, the aim of this work is to study the effect of surfactant removal on MSN by calcination at different temperatures (400 °C, 450 °C, 500 °C and 550 °C) or by extraction with HCl/ethanol or NH_4NO_3/ethanol. The final materials are fully characterised by different techniques. The study performed shows the removal efficiency when the different methods are used, and their effect on silica condensation degree, mesoporosity, cytotoxicity, and degradation rate. The results allow for obtaining a deeper knowledge of the surfactant removal processes.

1. Introduction

Mesoporous silica nanoparticles (MSN) are versatile materials that can be applied in different fields such as, among others, nanomedicine [1,2], drug and gene delivery [3,4], chemical communication [5,6], nanomotors [7,8], sensing [9,10], antimicrobial activity [11], catalysis [12], and gas storage [13]. Using surfactant as a scaffold is essential to synthesise MSN by a template-directed method. Nevertheless, once MSN are formed, eliminating the surfactant is required in almost all cases to empty the pores and house compounds such as active pharmaceutical ingredients, catalysts, dyes, etc. In addition, effective surfactant elimination is crucial for the application of MSN in biomedicine because of the toxicity of most of the surfactants. This is especially relevant in the case of CTAB, which is used as a surfactant in the synthesis of MCM-41-type MSN and whose toxicity is high even at residual concentration [14–16]. In this context, different methods to eliminate the surfactant have been reported, such as calcination, extraction, or dialysis. Regarding the procedure employed, the properties of the nanoparticles can be strongly affected. Some parameters influenced by the elimination procedure are the surfactant elimination efficiency [16,17], the silica condensation degree, the degradation rate [18], the mesoporosity [17,19], and aggregation phenomena [20–22].

* Corresponding author. Instituto Interuniversitario de Investigación de Reconocimiento Molecular y Desarrollo Tecnológico (IDM), Universitat Politècnica de València, Universitat de València, Camino de Vera s/n, 46022, Valencia, Spain.
** Corresponding author. Instituto Interuniversitario de Investigación de Reconocimiento Molecular y Desarrollo Tecnológico (IDM), Universitat Politècnica de València, Universitat de València, Camino de Vera s/n, 46022, Valencia, Spain.
*** Corresponding author. Instituto Interuniversitario de Investigación de Reconocimiento Molecular y Desarrollo Tecnológico (IDM), Universitat Politècnica de València, Universitat de València, Camino de Vera s/n, 46022, Valencia, Spain.
E-mail addresses: vicanno@etsid.upv.es (V. Candela-Noguera), mmarcos@qim.upv.es (M.D. Marcos), rmaez@qim.upv.es (R. Martínez-Máñez).

https://doi.org/10.1016/j.micromeso.2024.113119
Received 8 January 2024; Received in revised form 15 March 2024; Accepted 5 April 2024
Available online 7 April 2024

Calcination is the most frequently applied method due to its simplicity and effectivity, which is based on the thermal treatment of samples in order to provoke the combustion and oxidation of the surfactant [23]. In the case of non-ionic copolymer surfactants, the temperature employed is in the range of 300–350 °C [18,24]. However, cationic surfactants, such as the CTAB, are more difficult to remove. Hence, higher temperatures in the range of 450 °C–600 °C are required, as lower ones lead to incomplete CTAB decomposition [16,24,25]. In this context, the most frequently reported calcination temperature to remove the CTAB in MSN is 550 °C ([26,27]). Additionally, during the calcination process, the silicate framework is consolidated via thermal condensation of silanol groups and the elimination of structural defects [23,28]. This consolidation results in stronger and more stable materials [18]. Nevertheless, the calcination and the consequent consolidation of the framework has also negative implications [18,29], such as the reduction of silanol groups compared to the as-made samples [23] that reduces the reactivity of MSN surface [18]. Furthermore, high condensation of silanols provokes significant network shrinkage, which can impair the mesostructured framework of MSN [18,30,31]. Apart from this, it is also reported that calcination induces significant agglomeration of nanoparticles due to the formation of interparticle bonds [20–23, 29].

Solvent extraction procedure was developed to avoid the disadvantages of calcination [32]. It consists of the elimination of surfactant by washing the MSN with specific solutions and temperature. The solutions employed must be able to weaken the bonds between the silica surface and the surfactant. In the case of ionic surfactants, the ionic exchange is required to replace the electrostatic interactions between the silica and the surfactant. For this purpose, the solutions prepared to remove CTAB include a cation by which CTA^+ is substituted, such as those derived from HCl [15,16,33], NaCl [34,35] or NH_4NO_3 [14,36,37]. On the other hand, the solvents used are those in which the surfactant is strongly soluble. In the case of CTAB, the most commonly used are ethanol [38] and methanol [39], but other solvents can also be used, such as 1, 4-dioxane [40]. Regarding the effectiveness of complete template removal, some studies report that the extraction with NH_4NO_3 or HCl completely removes the FTIR bands associated with CTA^+ [16,39, 41–43], although, other studies differ [15,17,23,28,40] and report some associated cytotoxicity attributed to the presence of CTAB residues [19]. Furthermore, the use of an extraction method provokes a lower silanol condensation than that obtained by calcination [22]. Extraction is also a less aggressive method that induces lower shrinkage of the network. As a counterpart, extracted materials are less consolidated and lack hydrothermal stability [28].

Alternative methods have been developed to find suitable surfactant removal procedures according to the applications of the materials. For example, some authors have applied dialysis to remove the template. This procedure is mainly based on the same principles as solvent extraction. However, it uses a dialysis membrane to retain the nanoparticles and facilitate the sequential renewal of the solvent to shift the equilibrium and force the exchange and removal of the surfactant. The solution most commonly employed is acetic acid in ethanol [44,45], but other compounds such as NaCl [46] or solvents such as 2-propanol [47] have also been used. Dialysis method is reported to be effective in the complete elimination of surfactant [48,49]. Other advantages of using this method are that the silica framework barely varies after being dialysed and the silanol condensation is quite limited [44], although the main benefit is its compatible use with colloidal and dispersed MSN, since it avoids the drying-resuspension cycles and the sharp changes in solvent or solutions [22,45,48]. Nevertheless, the dialysis process is steeply time-consuming, in the range of several days to weeks. Moreover, it requires a large amount of solvents, which limits its use and costs for scalable production [39]. Other less common methods have also been developed for surfactant removal, including oxidation with hydrogen peroxide [50], ether cleavage [23], pyrolysis in N_2 flow [24], methanol-enhanced supercritical CO_2 extraction [51], non-thermal plasma oxidation [30,52], and other methods derived from calcination, such as rapid calcination or microwave-assisted calcination [23] or liquid-phase calcination [20].

Despite the large amount of work related to the extraction of the surfactant from MSN, there are still discrepancies in the literature. Furthermore, the greater part of the research has focussed on evaluating the efficiency of the method or the ease and scalability. Thus, there are recent reviews that show, with this perspective and in an extensive manner, a plethora of different surfactant elimination strategies [53]. However, there are considerably fewer studies that have addressed the question of what happens to the silica after the surfactant has been removed. This aspect is crucial as the resulting silica is the material that is later used in different applications. Depending on the specific use or application, the requirements for MSNs may be different. Hence, removal can be perceived not only as a stage in processing but also as a method of modulation of the properties of the resulting MSNs to achieve better adaptation to their use. In this context, our objective was to carry out a systematic study of the use of different surfactant removal procedures on standard MCM-41-type MSN and the implications on the final nanoparticles in terms of the silica condensation degree, the silica network and mesoporosity, the cytotoxicity, and the biodegradation rate. The methods we test are the most used, simple, and scalable: calcination at different temperatures (400, 450, 500, and 550 °C) and solvent extraction by using HCl-ethanol or NH_4NO_3-ethanol mixtures. Our study aims to provide a comprehensive and detailed insight into the implications of the use of different surfactant removal methods on the characteristics of MSN, especially in a biomedical context, such as drug delivery, imaging, or tissue engineering, in which the biocompatibility and biodegradability are crucial.

2. Materials and methods

2.1. Chemicals

The compounds tetraethylorthosilicate (TEOS, 98%), 1-hexadecyltrimethylammonium bromide (CTAB, 99%), sodium hydroxide (NaOH, ≥98%, anhydrous pellets), Dulbecco's Phosphate Buffered Saline (PBS, 275–304 mOs/kg), ammonium nitrate (NH_4NO_3, ≥98%), were purchased from Sigma-Aldrich. Hydrochloric acid (HCl, 37%)and absolute ethanol (≥99%) were purchased from Scharlab.

2.2. General techniques

Transmission electron microscopy (TEM) images were acquired in a JEOL JEM-1400 Flash microscope (Jeol Europe SAS, Croissysur-Seine, France). A Bruker D8 Advance diffractometer (Cu Kα radiation) (Bruker, Coventry, UK) was used for powder X-ray diffraction (PXRD) measurements. Solid-state nuclear magnetic resonance (ss-NMR) studies were performed in a Bruker Avance III 400 WB (Bruker, Coventry, UK). A micromeritics ASAP 2010 automated analyser was used for recording of N_2 adsorption–desorption isotherms (Micromeritics, Norcross, GA, USA); samples were degassed at 120 °C in vacuum overnight, the specific surface areas were calculated from the adsorption data within the low-pressure range using the BET (Brunauer–Emmett–Teller) model and the pore size distribution was determined following the BJH (Barrett–Joyner–Halenda) method. Particle size and ʒ potential in solution were measured by ZetaSizer Nano ZS (Malvern Instruments Ltd., Malvern, UK) equipped with a laser of 633 nm and collecting the signal at 173°. FTIR measurements were taken by a Bruker Tensor 27 spectrometer (Bruker, Coventry, UK). Thermogravimetric analyses were carried out on a TGA/SDTA 51e balance (Mettler Toledo Inc., Schwarzenbach, Switzerland) in an oxidizing atmosphere (air, 80 mL min-1) with a heating rate program between 25 and 1000 °C at 10 °C min-1, with an isothermal heating step at 100 °C for 1 h and a final isothermal at 1000 °C for 30 min.

2.3. Synthesis of nanoparticles

1 g of CTAB (2.74 mmol) was mixed with 480 mL of deionised water in a 1 L (10.5 cm of outer diameter) cylindrical beaker. The mixture was heated at 50 °C and stirred with a cylindrical and plain magnetic stir bar (60 mm long and 15 mm diameter) at 500 rpm to dissolve the surfactant. Then, 280 mg of NaOH (7 mmol) dissolved in 3.5 mL of deionised water were added, and the temperature solution was adjusted to 80 °C. A watch glass was placed to cover the beaker to minimize the evaporation solvent and therefore to avoid volume decreasing during the reaction. When the temperature reached 80 °C, 5 mL of TEOS (25.7 mmol) were added dropwise, using a syringe and a needle. Soon after, a white precipitate appeared. The mixture was stirred for 2 h. After this time, the suspension was cooled at room temperature, and the solid product was vacuum filtered in a Buchner filtering device over a filter paper (Whatman™ Grade 3 MM Chr), and deionised water was added until neutralising the suspension. Then, the solid was dried under vacuum and ground to obtain a white powder, named **MSN-as made.**

2.4. Surfactant removal

After the synthesis, different methods were employed to remove the surfactant. Calcination: **MSN-as made** was calcined in a ventilated oven (oxidant atmosphere) for 5 h at 400, 450, 500, and 550 °C, to obtain respectively **MSN-400**, **MSN-450**, **MSN-500,** and **MSN-550**. Extraction: the solid was extracted using different solvents. First, 300 mg of the **MSN-as made** solid were suspended and briefly sonicated in 6 ml of fuming HCl in 100 ml ethanol. The suspension was refluxed for 2 h and washed with ethanol three times. Three cycles of refluxing-washing were performed. The solid was dried for 24 h at 37 °C and finally ground. The obtained material was called **MSN-extHCl**. A similar procedure was followed for the surfactant extraction with ammonium nitrate, where the extracting solution was prepared with 2 mg of NH_4NO_3 in 100 ml of ethanol. The solid obtained was called **MSN-extNH_4NO_3**.

2.5. DLS measurements

Dynamic light scattering (DLS) technique was used to measure the hydrodynamic size of the nanoparticles. For DLS measurements, the samples were prepared by suspending and sonicating generously the nanoparticles in distilled water (1 mg NP/ml) and spinning them briefly (at 10,000 rpm) to remove the presence of large aggregates or sedimentation. Electrophoretic light scattering (ELS) technique was used to measure the ζ potential of the nanoparticles, which is related to their surface charge. For ELS measurements, the samples were prepared by suspending and sonicating generously the nanoparticles in distilled water (10 mg NP/ml) and spinning them briefly (at 10,000 rpm) to remove the presence of large aggregates or sedimentation, which would have disturbed the electrophoretic movement measurements.

2.6. Biocompatibility assays

The *in vitro* cytotoxicity assays were performed on human brain glioblastoma cells (LN-18). Cell culture was incubated in Dulbecco's Modified Eagle Medium (DMEM) high glucose supplemented (Sigma-Aldrich) with 10% of serum foetal bovine (SFB) (Sigma-Aldrich) and in 5% CO_2 at 37 °C and underwent passage twice a week. The nanoparticles used to treat the cells were suspended and generously sonicated in DMEM-SFB. Cells were treated for 4 h and incubated with fresh media. At 72 h, 10 μL of WST-1 reagent (Roche Applied Science) were added to each well (in a 96-well microtiter plate) and were incubated for 1 h at 37 °C. The absorbance, directly related to cell activity, was read at 440 nm. Cell viability measurements were taken in a Wallac 1420 Victor2 Microplate Reader (Perkin Elmer, Waltham, MA, USA).

2.7. Degradation assays

Nanoparticles were suspended at 1 mg/mL concentration in PBS and generously sonicated. Then, the suspension was stirred with a magnetic stirrer for 2 weeks at room temperature. Small aliquots (50 μL) were collected after 1, 4, 7, and 14 days, and studied by transmission electron microscopy. After collecting each aliquot, the nanoparticles suspension was centrifuged and then resuspended in fresh PBS to avoid saturation of the silicic acid on the media and facilitate the degradation process.

2.8. Image analysis

TEM images were used to analyse the properties of MSN, such as their size or mesoporosity. At least 200 particles for each sample were counted to obtain the average diameter and the percentage of nanoparticles with mesoporosity. Nanoparticles were considered to possess mesoporosity only if clear hexagonal ordering of the pores or parallel channels could be observed.

3. Results and discussion

3.1. Synthesis of nanoparticles and surfactant removal

MCM-41-type MSN were synthesised according to the protocol described in the experimental section. 1.85 g of the as-made solid obtained (**MSN-as made**) was then divided into six vials and different methods were used to remove the surfactant. Nanoparticles of four of the vials were calcined at different temperatures (400 °C, 450 °C, 500 °C and 550 °C) to obtain samples **MSN-400**, **MSN-450**, **MSN-500** and **MSN-550**. Besides, nanoparticles from the two remaining vials were treated with ethanol:HCl or ethanol:NH_4NO_3, leading to **MSN-extHCl** and **MSN-extNH_4NO_3** samples.

The calcination temperatures employed were chosen to compare the standard calcination (at 550 °C) with other temperatures. The lower limit was set at 400 °C according to the temperature in which the CTA^+, when acting as a template, is reported to be mostly calcined [54–57]. Under our experimental conditions, some differences were observable to the naked eye between the calcinated samples (Fig. 1). The solid calcined at 400 °C (**MSN-400**) showed a beige colour, whereas samples calcined at temperatures above 500 °C were obtained in the form of a white powder. **MSN-450** also showed a light beige appearance (barely observed in Fig. 1). On the other hand, both extracted solids (**MSN-extHCl** and **MSN-extNH_4NO_3**) were also obtained in the form of a white powder, which were finer than the ones obtained by calcination.

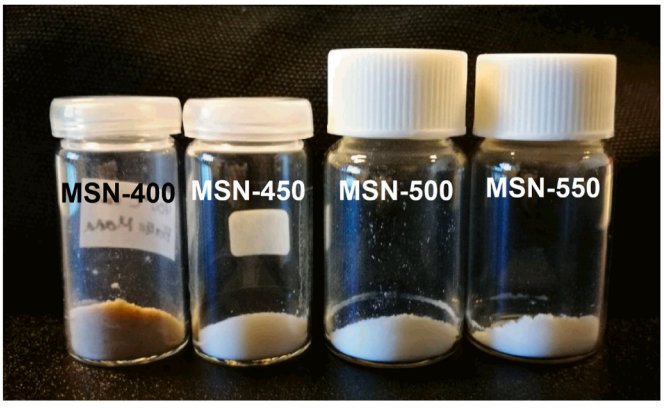

Fig. 1. Photograph of calcined samples MSN-400, MSN-450, MSN-500, and MSN-550.

3.2. Study of surfactant removal efficiency

The different methods employed to remove the surfactant template were compared in terms of their removal efficiency. For this purpose, both thermogravimetric analysis (TGA) and Fourier-transform infrared spectroscopy (FTIR) were used. First, calcined samples were analysed. Their TGA curves and FTIR spectra are plotted together with those of **MSN-as made** in Fig. 2A and B, respectively. The TGA results (Fig. 2A) are shown as the percentage of the dry solid (removing from the initial weight the contribution of moisture and other solvents) as a function of temperature, according to considerations previously reported [58,59]. Therefore, the loss of weight observed can be associated with the decomposition of organic matter and silanol condensation. **MSN-as made** had a total weight loss of 45.9%. The tendency observed in the curve can be divided into three areas (Fig. 2A, dashed lines). Firstly, there is a sharp drop from 180 °C to 360 °C, representing a weight loss of 39%; secondly, there is a less steeply sloping weight loss from 360 °C to 550 °C, representing 4.5%; and finally, above 550 °C (up to 1000 °C) the weight loss is much less steep, and there is only a 2.5% weight reduction. In contrast, the percentage of weight loss in calcined samples is much lower, and this percentage decreases with calcination temperature. Thus, the calcined samples showed a total weight loss of 5.6%, 4.1%, 3.8%, and 3.4%, for **MSN-400**, **MSN-450**, **MSN-500,** and **MSN-550**, respectively, which are in the range reported in the literature [58,59]. The difference between the last three samples (**MSN-450**, **MSN-500** and **MSN-550**) is less than 1% and their curves are barely distinguishable in Fig. 3A (yellow, orange, and red lines, respectively). In the case of **MSN-400**, the difference is larger, as it shows a more pronounced decay in the range from 360 °C to 550 °C, from which the curve separates from the rest (Fig. 2A, light green line).

FTIR spectroscopy of **MSN-as made** was used to check the presence of bands associated with the CTA $^{+}$ molecules (Fig. 2B, dotted lines). According to the literature and our observations in **MSN-as made**, these bands are located approximately at 2959, 2918, and 2850 cm^{-1} (stretching bands from methylene (–CH_2–) and methyl groups (-CH_3)), 1470 and 1400 cm^{-1} (bending bands from –CH_2- and –CH_3) and 724 cm^{-1} (rocking band from –CH_2-) [60]. Only alkane related peaks of CTA^+ can be observed in FTIR spectroscopy, as quaternary amines lack of signals. The spectra of calcined samples (**MSN-400**, **MSN-450**, **MSN-500,** and **MSN-550**) show the bands associated with the silica matrix but not with the CTA^+ molecules, regardless of the calcination temperature used.

According to the observations made by naked eye (*vide ante*), the beige appearance of **MSN-400**, and **MSN-450** to a lesser extent, suggests the presence of some CTA^+ residues. Nevertheless, as FTIR results showed no signals associated with CTA^+ in the four calcined samples, we hypothesise that the residues remaining in **MSN-400** and **MSN-450** are coke residues, whose FTIR signals are negligible [61,62]. Coke residues are reported to remain in the MSN when the calcination process is not complete [25,63,64], and the presence of even 1% by weight of coke residues may explain the beige appearance. Hence, we can only claim that CTA^+ and its residues are completely removed, under our experimental conditions, from 500 °C. In this context, there is no consensus in the literature about the minimum temperature necessary to remove completely the CTA^+ from the mesopores, which varies from 350 °C to 600 °C [24,65–67].

For their part, TGA curves show a progressive decrease in weight loss with increasing calcination temperature (*vide ante*). This can be produced by a double phenomenon. On the one hand, as the temperature increases the coke residues still present in calcined samples are removed. On the other hand, the silanol groups, which are quite abundant in MSN prior to surfactant extraction, are progressively condensed when increasing the calcination temperature [41]. In this context, some authors described that the condensation reaction occurs from 400 °C [18,30]. Nevertheless, Potapov et al. [68] analysed the silanol condensation as a function of the temperature applied on precipitated amorphous silica, and they reported silanol condensation at even lower temperatures. The authors described that silanol condensation occurs in three stages depending on the type of the silanols involved, their location inside the silica framework and the proximity between them: 1) from 190 to 400 °C the vicinal and geminal –OH groups are condensated, 2) from 400 to 780 °C the main contribution is due to condensation of free nearby individual –OH groups, and 3) above 780 °C the condensation is limited to the widely spaced –OH groups.

Therefore, the three areas in the TGA curve of **MSN-as made** can be associated with specific phenomena. The sharp drop from 180 °C to 360 °C is roughly the region where CTA + has been reported to decompose [34,69,70] and most of the vicinal and geminal –OH groups condense. Subsequently, the weight lost from 360 °C to 550 °C can be associated with the combustion of CTA^+ residues and the condensation of a portion of nearby silanol groups. Finally, from 550 °C the weight loss can be exclusively attributed to the condensation of the remaining Si–OH groups. In this sense, the percentage of weight decrease in **MSN-550** (3.4%) can be associated exclusively with the presence of silanol groups. For the rest of the calcined samples, **MSN-400**, **MSN-450,** and **MSN-500**, the weight loss exceeds that of the **MSN-550** sample in a 2.2%, 0.7%, and 0.4%, respectively. These percentages can be assumed to correspond to the presence of additional silanol groups in comparison with **MSN-550**, or the presence of some coke residues in the case of **MSN-450**, and especially, **MSN-400**.

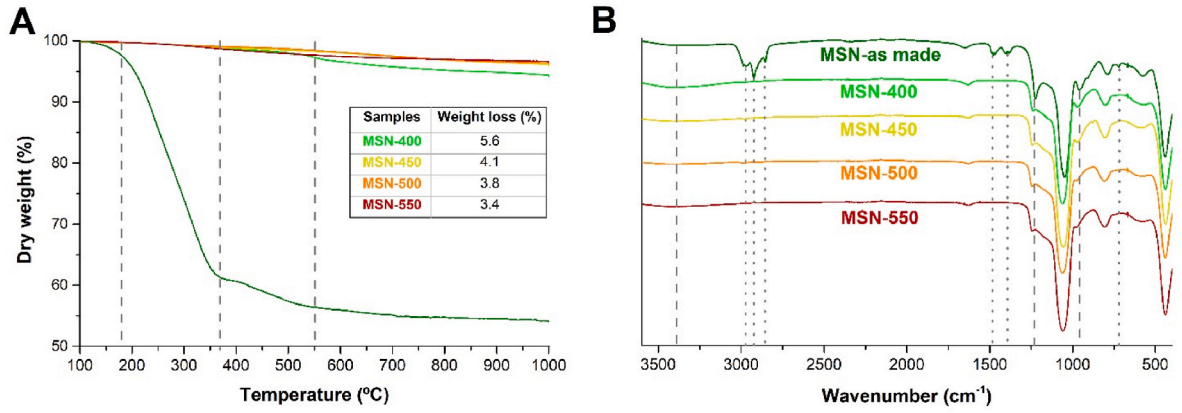

Fig. 2. Surfactant removal efficiency of calcination at different temperatures. (A) TGA curves of calcined and as-made samples. Dashed lines indicate the three different stages in weight loss. The values of weight were expressed according to the percentage of the dry solid (removing from the initial weight the contribution of moisture and other solvents). (B) FTIR spectra of calcined and as-made samples. Dotted lines indicate the CTA^+ associated FTIR bands. Dashed lines indicate the Si–OH and flexibility associated lines. The colors used in both graphs are correlated.

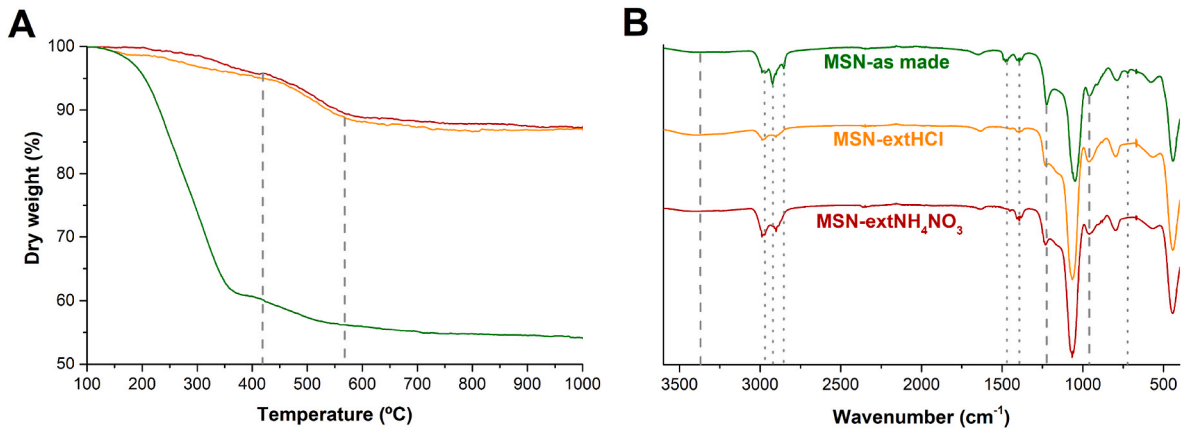

Fig. 3. Surfactant removal efficiency of extraction methods. (A) TGA curves of extracted and as-made samples. Dashed lines indicate the region in which the thermal decomposition is greater in extracted samples. The values of weight were expressed according to the percentage of the dry solid (removing from the initial weight the contribution of moisture and other solvents). (B) FTIR spectra of extracted and as-made samples. Dotted lines indicate the CTA^+ associated FTIR bands. Dashed lines indicate the Si–OH and flexibility associated lines. The colors used in both graphs are correlated.

In summary, it can be concluded that the efficiency of surfactant removal is optimal by calcining above 500 °C. In addition, a progressive condensation of silanols is supposed to take place above 190 °C, according to the observations and the reported literature.

TGA curves (Fig. 3A) and FTIR spectra (Fig. 3B) of extracted solids (**MSN-extHCl** and **MSN-extNH_4NO_3**) were also studied in comparison with those of **MSN-as made**. The TGA results (Fig. 3A) show a weight loss of 13.1% for **MSN-extHCl** and 12.6% for **MSN-extNH_4NO_3**. Even though these percentages are lower than those observed for the **MSN-as made**, they are higher than those found for the calcined samples. Similar behaviours were observed in other reported studies, which described a weight loss of ca. 10% in TGA curves for MSN extracted with NH_4NO_3, NaCl, or HCl in ethanol or methanol [14,34,42]. The TGA curves for both extracted samples show the most significant weight reduction from 420 °C to 570 °C (Fig. 3A, dotted lines), in which they lose around 7% matter.

Regarding the FTIR spectra (Fig. 3B), both extracted samples, **MSN-extHCl** and **MSN-extNH_4NO_3**, show the disappearance of most of the CTA^+ associated FTIR bands (Fig. 3B, dotted bands), such as the signals at 720, 1470, 2850, and 2918 cm^{-1}. Nevertheless, the bands at 1400 cm^{-1} (bending bands from $–CH_2$- and $–CH_3$) and 2959 cm^{-1} (stretching bands from $–CH_2$- and $–CH_3$) remain present in both samples. Additionally, other peaks in the 3000 cm^{-1} region are also observed, such as those at 2900 and 2980 cm^{-1}.

TGA curves seem to suggest that the observed weight loss above 420 °C is not primarily due to the presence of surfactant, as the removal of surfactant is mainly produced at lower temperatures (from 180 °C). FTIR spectra also indicate that the bands found do not correspond to CTA^+. Then, the observed weight loss could be mainly attributed to the condensation of a high amount of silanol groups that remain in the extracted samples. Nevertheless, it has been reported that the percentage of silanol groups in extracted samples is close to 5% of the nanoparticle's weight [59], whereas we observed percentages above 10%. In addition, the FTIR spectra suggest the presence of other residues in the extracted samples, which can also contribute to the high percentage of weight loss. In concert with that, it can be hypothesised that the observed bands may be better assigned to ethanol traces (whose bands appear at 1384 and 2980 cm^{-1}). However, this cannot explain the main weight decrease found in TGA, since ethanol evaporation is located below 100 °C. Thus, it is suggested that the bands at 2980, 2959, 2900, and 1400 cm^{-1} correspond to the presence of ethoxy moieties [71], which are formed during the solvent extraction by esterification of some silanol groups [23,29], which can be produced in acidic ethanol suspension at refluxing conditions [72].

Consequently, it can be suggested that the extraction methods employed remove completely the CTA^+ from MSN. Nevertheless, both extractions with HCl/ethanol and NH_4NO_3/ethanol lead to nanoparticles with ethoxy groups attached to the surface.

3.3. Analysis of condensation degree of the MSN

The proportion of silanol groups in the MSN plays an important role in some properties of the MSN such as their surface reactivity [19], polarity [50], adsorption capacity [19,54,68] or toxicity and haemolytic activity [73,74]. For this reason, it is important to study the effect of different methods of surfactant removal on the degree of condensation of the silica matrix. For this purpose, FTIR spectra were analysed again focusing on the bands related to the silica framework (Figs. 2B and 3B, dashed lines). Additionally, ^{29}Si-ss-NMR measurements (Fig. 4 and Table 1) were performed to study the silica connectivity. Third, ELS measurements were analysed to study the ζ potential of the samples (Table 1), considering that the negative charge of MSN comes from the deprotonated silanols (silanolates, $Si–O^-$) on the surface.

Starting with the FTIR spectra, the bands related to the condensation degree of the MSN silica matrix are those associated with the Si–OH group (stretching broad band at 3400 cm^{-1} of the O–H bond and bending band at 954 cm^{-1} of Si–OH bond) and the one associated with Si–O–Si bonds flexibility (the shoulder at 1217 cm^{-1} due to bending vibrations) [24,75,76].

In the case of the calcined samples, it can be observed (Fig. 2B, dashed lines) that the bands associated with the Si–OH bonds (at 3400 and 954 cm^{-1}) decrease progressively as the calcination temperature increases compared with **MSN-as made**, especially above 500 °C. In the same vein, the shoulder at 1217 cm^{-1}, which is quite sharp in **MSN-as made**, is highly reduced in all the calcined samples, suggesting the calcination must produce a high increment of the framework rigidity. On the other hand, the FTIR spectra of the extracted samples (Fig. 3B, dashed lines) reveal that the bands associated with the Si–OH and O–H vibrations (3400 cm^{-1}, 954 cm^{-1}) were not so reduced in comparison with calcined samples, neither the stretching nor bending Si–O–Si vibrations (1217 cm^{-1}). The higher amount of silanols in extracted samples can be explained additionally due to the rehydroxylation of condensed siloxane groups, which can occur at favourable conditions, such as acidic or alkaline pH, high temperature and aqueous solutions [23,68].

On the other hand, ^{29}Si-ss-NMR spectroscopy was used to quantify the connectivity of silica, namely, the percentage of the Q^2, Q^3 and Q^4 signals in the samples, localised at ca. −91, −101, and −111 ppm, respectively. These signals are closely related to the silica condensation degree and the presence of silanol groups: geminal silanol groups in the

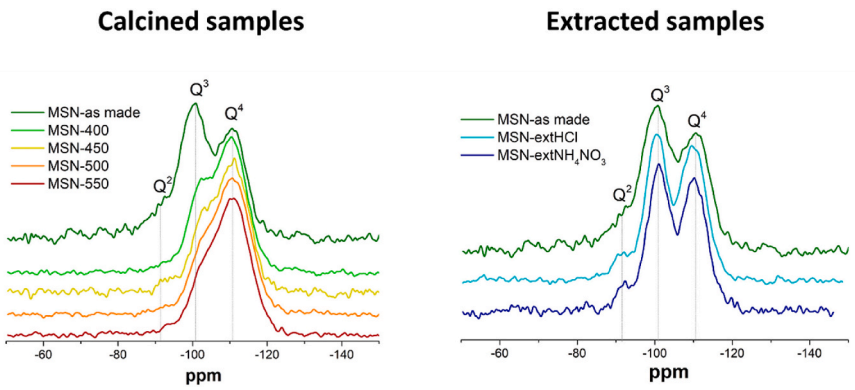

Fig. 4. Si^{29}-ss-NMR spectra of as-made, calcined (**MSN-400**, **MSN-450**, **MSN-500**, **MSN-550**) and extracted **(MSN-extHCl** and **MSN-extNH$_4$NO$_3$**) samples. Dotted lines indicate the Q^2, Q^3 and Q^4 signals.

Table 1
Data related to the silica condensation degree (ζ potential and percentage of the Q^2, Q^3, and Q^4 peaks with respect to the total ss-NMR signal) for the samples obtained by using different surfactant removal methods.

SAMPLE	ζ POTENTIAL (mV)	Si^{29}-ss-NMR			
		% Q^2	% Q^3	% Q^4	Degree of condensation (DC)
MSN-as made	+33.5 ± 3.2	9.6	49.3	41.1	82.9
MSN-400	−33.8 ± 1.4	4.1	26.0	69.9	91.5
MSN-450	−35.5 ± 2.4	4.0	23.6	72.4	92.1
MSN-500	−36.8 ± 1.5	3.5	21.3	75.2	92.9
MSN-550	−32.9 ± 1.7	3.1	20.1	76.8	93.4
MSN-extHCl	−38.1 ± 0.9	7.0	42.1	51.0	86.0
MSN-extNH$_4$NO$_3$	−37.6 ± 1.2	6.9	43.8	49.3	85.6

case of Q^2 silicon centres (=Si-$(OH)_2$), isolated silanol groups for Q^3 type centres (≡Si–OH) and siloxane bonds for Q^4 type centres (≡Si–O–Si≡). The area under the curve (AUC) was calculated for each peak by deconvolution of the spectra according to a Gaussian distribution. ^{29}Si-ss-NMR spectra of calcined and extracted samples in comparison to **MSN-as made** are shown in Fig. 4 and the obtained data are collected in Table 1. The calcined samples showed a strong reduction in Q^2 and Q^3 signals, even in samples calcined at 400 °C. In addition, there is a correlation between the temperature of calcination and the increase in the degree of condensation, calculated according to the equation reported by Barczak [23] (Table 1). The results were consistent with previously reported data [18,23,50,63,77]. On the other hand, the NMR spectra of extracted samples showed a slight reduction of Q^2 and Q^3 signals, and then, a smaller increase in the degree of condensation when compared with the **MSN-as made** sample.

Regarding the ζ potential (Table 1), it increases when increasing the calcination temperature from 400 to 500 °C (-33.8 < - 35.5 < - 36.8 mV) but decreases at 550 °C (-32.9 mV). A tentative explanation for this experimental observation is that the presence of surfactant residues (coke) in the nanoparticles may soften the negative charge that **MSN-400** and **MSN-450** should have due to silanol/silanolate groups. Moreover, raising the calcination temperature increases the condensation of silanol/silanolate groups and, therefore, the negative charge is reduced, which is the trend observed for **MSN-500** and **MSN-550**. For their part, the ζ potential values for extracted samples were −38.1 and −37.6 mV for **MSN-extHCl** and **MSN-extNH$_4$NO$_3$**, respectively. These values are more negative than for any calcined sample, in agreement with a higher number of silanol/silanolate groups in the extracted samples.

According to the data obtained in FTIR, ^{29}Si-ss-NMR and ELS, it can be concluded that the use of increasing calcination temperatures leads to the increase of the silica condensation degree and the reduction of silanol groups. In addition, the extraction method produces a lower condensation degree compared with calcination, regardless of the temperature used. In the same vein, the framework flexibility is less affected by extraction than by calcination.

3.4. Mesostructured framework shrinkage

The framework shrinkage was also mentioned as one of the most affected parameters in relation to the surfactant removal method. Nevertheless, no agreement is found in the literature concerning the effect of surfactant removal on the mesostructured framework. First studies on mesoporous materials in the '90s reported calcination at lower temperatures, such as 500 °C [63,78,79], but no studies on the implications on the silica framework were carried out. Other authors reported different calcination temperatures in KIT-6 and SBA-15 materials and they reported that the specific surface area and pore volume were optimised at intermediate temperatures, where the surfactant was completely removed, but the shrinkage was less pronounced [18]. Some reports indicated that calcination leads to smaller pore size and volume in comparison with extraction procedures, due to the sharp shrinkage provoked by calcination [23,29,80]. Conversely, Hudon et al. [16] reported that the extraction with ethanol-HCl leads to a lower surface area in comparison with calcined samples. Similarly, He et al. [38] reported a specific surface area of ca. 863 m^2/g, which is quite low, in MCM-41-type MSN extracted with HCl:ethanol reflux. In this case, it can be hypothesised that the surface reduction is not provoked by the extraction method by itself but by the application of the ethanol washing immediately after the formation of the nanoparticles, whose silica framework is still weak just after their synthesis [81]. Considering that, the ethanol washing can dissolve a part of the CTA^+ molecules that are inside the pores and provoke a strong shrinkage of the unconsolidated silica framework.

Hence, the porosity of calcined and extracted samples was studied. First, PXRD was performed and analysed. The diffraction patterns of calcined and extracted samples (Fig. 5A) present the peaks observed in

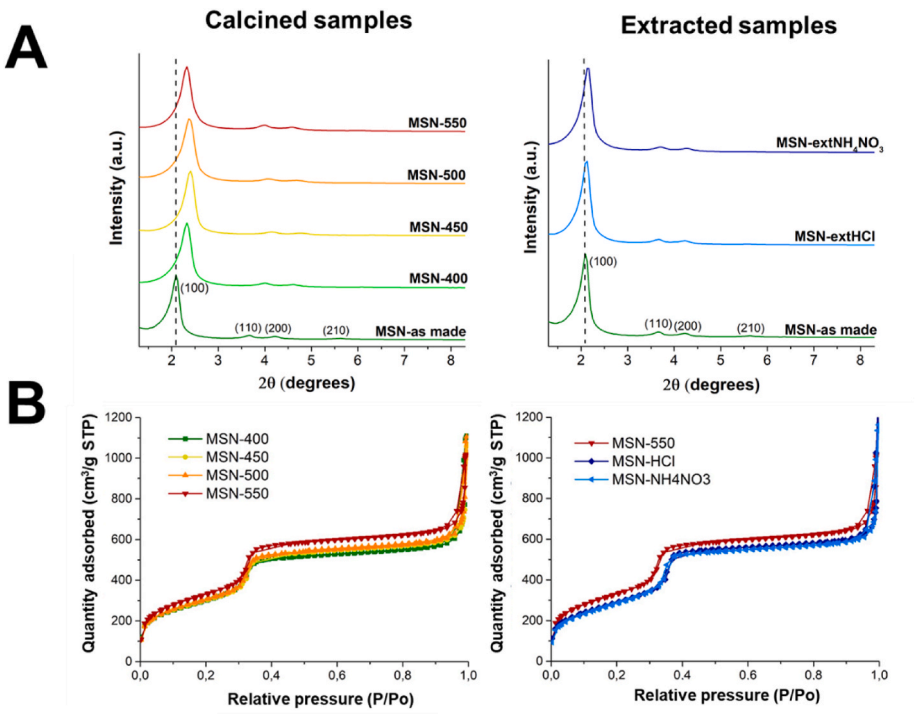

Fig. 5. A) PRXD patterns of calcined and extracted samples in comparison to **MSN-as made**. Dotted lines indicate the position of (100) in **MSN-as made**. Miller's indexes of crystallographic family planes are indicated in parenthesis. B) N_2 absorption-desorption isotherms of calcined and extracted samples compared to **MSN-550**.

Table 2
Crystallography data of samples obtained with the different surfactant removal methods. (FWHM ratio: width of the (100) peak in calcined and extracted samples related to the width of this same peak in the as-made sample).

SAMPLE	Peak (100) (2θ)	d_{100} (nm)	Unit cell (nm)	Unit cell contraction (nm)	$FWHM_{100}$	$FWHM_{100}$ ratio
MSN-As made	2.09	4.23	4.88	–	0.22	–
MSN-400	2.31	3.82	4.41	0.47	0.28	1.27
MSN-450	2.40	3.68	4.25	0.63	0.27	1.23
MSN-500	2.38	3.71	4.28	0.60	0.31	1.41
MSN-550	2.34	3.77	4.35	0.53	0.28	1.27
MSN-ExtHCl	2.11	4.19	4.84	0.04	0.25	1.14
MSN-ExtNH_4NO_3	2.15	4.10	4.74	0.14	0.26	1.18

typical MCM-41 material, corresponding to crystallographic planes (100), (110), (200) and (210), though the peak assigned to the (210) planes is not always visible in the patterns due to its small intensity and the loss of long-range order after surfactant removal. The interplanar distance d_{100} (of the main peak (100)) was calculated by applying Bragg's law ($n \cdot \lambda = 2d \cdot \sin\theta$), and the unit cell for a hexagonal structure was also calculated ($a_0 = 2/\sqrt{3} \cdot d_{100}$) (Table 2). A considerable reduction in d_{100} when nanoparticles are calcined can be found. **MSN-as made** presents a d_{100} of 4.23 nm, while in calcined samples the d_{100} value is in the range from 3.68 to 3.82 nm. No clear correlation was found between the calcination temperature and d_{100} value. A similar observation was reported by Basso et al. [18]. In contrast, in extracted samples, the d_{100} value barely changes from the as-made sample, being 4.19 and 4.10 nm for **MSN-extHCl** and **MSN-extNH_4NO_3**, respectively. In this context, a clear difference in the unit cell contraction between the calcined and extracted samples is observed, which is in the range of 0.4–0.6 nm and 0.05–0.15 nm, respectively.

On the other hand, the full width at half maximum of peak (100) ($FWHM_{100}$) was measured for each sample, as well as the FWHM ratio as the width of the (100) peak in the calcined and extracted samples in relation to the width of the same peak in the as-made sample (Table 2). The data show an increase of $FWHM_{100}$ after the surfactant removal, regardless of the removal method employed. Besides, the $FWHM_{100}$ ratio was higher in the case of the calcined samples (ranging from 1.23 to 1.41) than in the extracted ones (ranging from 1.14 to 1.18).

According to these results, it can be concluded that the structure shrinkage occurs at temperatures as low as 400 °C. In addition, this phenomenon is more pronounced in calcined than in extracted samples, even at lower calcination temperatures, as it has been widely reported [23,29,30]. In other words, the use of temperatures above 400 °C affects the silica framework to a greater extent than the exposure to an organic solvent and refluxing temperatures (ca. 80 °C), in the case of **MSN-extNH_4NO_3** sample, or highly acidic conditions, in case of **MSN-extHCl**. This phenomenon is also observed in the increment of the structure disturbance and symmetry defects, which can also be found in the literature [82] and is indicated by the value of the $FWHM_{100}$.

The N_2 absorption-desorption isotherms (Fig. 5B) were also obtained to compare the mesoporosity of calcined and extracted samples. All measured samples showed the typical isotherm of MCM-41 material. Regarding the calcined samples, it is observable how the slope of the isotherms in the interval of the N_2 monolayer formation, which is related to the BET surface area, increases slightly as higher calcination temperatures are used. The capillary condensation, which represents the filling of the pores, is found at the same pressure in all the cases ($p/p_o = 0.31$). Nevertheless, the quantity of N_2 adsorbed at average pressures increases progressively with the rise of the calcination temperature,

Table 3
Porosity data of samples as a function of surfactant removal method.

SAMPLE	BET surface (m^2/g)	Pore size (nm)	Pore volume (cm^3/g)	Wall thickness (nm)
MSN-400	1096	2.83	0.97	1.58
MSN-450	1097	2.85	1.00	1.40
MSN-500	1115	2.83	1.01	1.45
MSN-550	1208	2.84	1.09	1.51
MSN-ExtHCl	1079	2.86	0.99	1.98
MSN-ExtNH_4NO_3	1086	2.80	0.97	1.94

which suggests an increase in pore volumes. The extracted samples show quite similar isotherms but have a lower slope in the N_2 monolayer adsorption region and a lower amount of N_2 adsorbed at average pressures than the standard calcined sample. In the case of the capillary condensation, the extracted samples show a jump slightly shifted to higher pressures ($p/p_o = 0.32$). The calculated data from the isotherms according to BET and BJH methods are shown in Table 3.

The specific surface area of calcined samples is slightly higher with increasing calcination temperature ($1096 < 1097 < 1115 < 1208\ m^2/g$), as it is also the pore volume ($0.97 < 1.00 < 1.01 < 1.09\ cm^3/g$). In contrast, the pore size remains the same in the calcined samples (in the range of 2.83–2.85 nm), and no correlation was found between the calcination temperature and the shrinkage effect, as it is shown by PXRD data. Regarding the extracted samples, the surface area is smaller than that of the calcined ones, 1079 and 1086 m^2/g for **MSN-extHCl** and **MSN-extNH_4NO_3**, respectively, as it is also the pore volume (lower than 1.00 cm^3/g in both cases). In contrast, the pore size is similar to that of calcined samples (in the range of 2.80–2.86 nm).

The wall thickness was also calculated to better understand the material's shrinkage phenomenon, by removing the pore diameter value from the unit cell (a_0) value. In the case of the calcined samples, this value ranges from 1.40 to 1.58 nm and there was not a clear correlation between the wall thickness and the calcination temperature. In the case of extracted samples, the calculated wall thickness is larger (in the range of 1.94–1.98 nm).

We can observe that, in the case of calcined samples, no differences in shrinkage and pore size were observed from 400 °C to 550 °C. Hence, the increase in the pore volume and BET surface might be provoked by a progressive elimination of surfactant as the calcination temperature increases, through which the pores are progressively emptied. In the case of extracted samples, the values of pore volume and BET surface are in the range of the sample calcined at 400 °C. These low values can be explained due to the thicker wall of both extracted samples, which supposes a decrease in the number of pores per mass of nanoparticles. Finally, it can also be remarked that the shrinkage observed in calcined samples, compared with those extracted, is not due to differences in pore size, whose values are similar in all samples, but rather to differences in wall thickness. In fact, the differences in wall thickness between extracted and calcined samples fit with the unit cell contraction (close to 0.5 nm). Therefore, it can be affirmed that the calcination does not mainly provoke the shrinkage by a pore size contraction, but by a decrease in the thickness of the wall as a result of an increase in silica connectivity and structure sintering.

3.5. Study of the biocompatibility of prepared NPs

The cytotoxicity of the synthesised samples was tested *in vitro*. In the literature, the study of the biocompatibility of calcined or extracted MSN samples have been widely reported in both *in vitro* and *in vivo* models [19,83,84]. However, to our knowledge, the biocompatibility of calcined bare MSN obtained at temperatures lower than that commonly used in the standard synthesis (550 °C) has not been tested. Regarding the extraction method, the literature is still controversial, since some studies report toxicity [14–16] for extracted MSN, but others show good biocompatibility, most likely due to the higher efficiency of surfactant removal [38,41].

In this context, we performed dose-response cytotoxicity assays with the solids **MSN-as-made**, **MSN-400**, **MSN-450**, **MSN-500**, **MSN-550**, **MSN-extHCl,** and **MSN-extNH_4NO_3** (Fig. 6). None of the calcined or extracted samples presented cytotoxicity, even at concentrations as high as 250 μg/ml. Only the **MSN-as made** was highly toxic for cells, even at the lowest MSN concentration (10 μg/ml), which demonstrates the high toxicity of CTA^+. These results suggest that the elimination of surfactant by calcination or extraction has been complete, and that the possible presence of the CTA^+ decomposition residues (in samples calcined at 400 and 450 °C) or ethoxy groups (in extracted samples) do not produce a measurable cytotoxic effect.

3.6. Biodegradability of calcined and extracted samples

The degree of silica polymerisation in MSN is closely related to its ability to be degraded [85,86], as silanol groups are the starting point for the degradation of the silica matrix by the nucleophilic attack of H_2O molecules [87,88]. Biodegradability is particularly relevant for drug delivery applications, for which it is necessary to obtain MSN that are stable for a period that allows them to be loaded with a drug, distributed in the body, reach the target organs and effectively release the drug into them [89]. On the other hand, the nanomaterial must be degraded and disposed of after its biomedical mission to avoid long-term accumulation in the body.

In several *in vitro* and *in vivo* assays MSN have been demonstrated to be biodegradable materials in physiological conditions [85,90]. Nevertheless, they tend to accumulate in reticuloendothelial (RES)-related organs, such as the liver and spleen, where their clearance can take several weeks or even months due to their low degradation rate [91,92]. In fact, certain studies reported some toxicity associated with the long-term accumulation of MSN [93,94]. Besides, the mechanism and kinetics of MSN degradation are complex processes that depend not only on the degree of condensation of the silica, but also on other specific properties of the nanoparticles themselves and the environment [95] such as their concentration [90,96], structure and surface [44,96,97], or

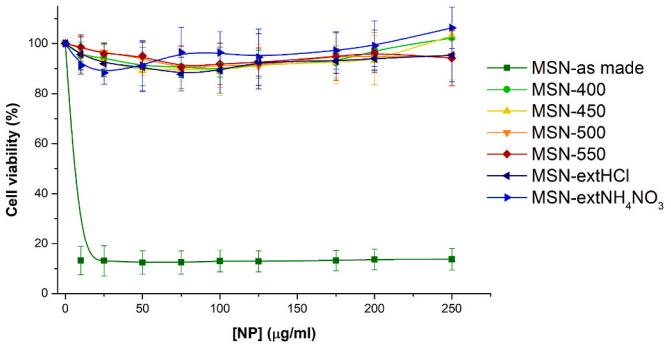

Fig. 6. Cell viability assay. Dose-response curves of LN-18 cells treated with different concentrations of calcined and extracted samples. Cell viability was measured with WST-1 reagent after 72 h of the addition of nanoparticles.

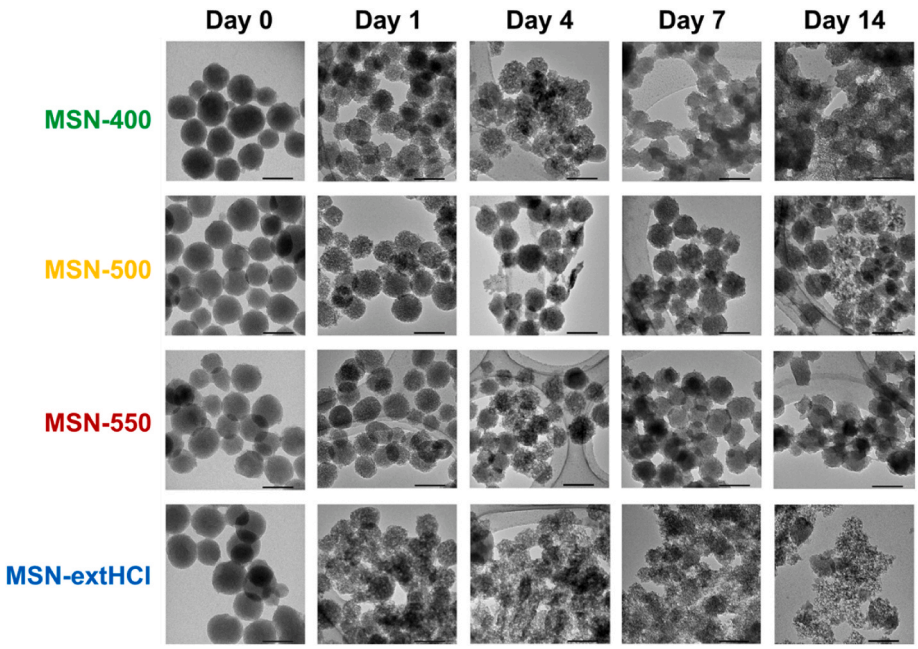

Fig. 7. Biodegradability assay. TEM images of **MSN-400**, **MSN-500**, **MSN-550,** and **MSN-extHCl** over time (0, 1, 4, 7, and 14 days). Nanoparticles were prepared at a concentration of 1 mg/mL in PBS and generously sonicated before starting the biodegradation assay. Scale bar = 100 nm.

functionalisation [98].

Some effective strategies to improve the MSN degradation have been attempted in the last years [85]. These approaches include modifying the nanoparticle's composition or surface as well as including stimuli-responsive bonds within the silica framework [99]. Regarding the surfactant elimination method, calcined samples are highly consolidated, and therefore, tend to show remarkably low degradation percentages [90,96,100,101] in comparison with extracted MSN, which present low structural consolidation [102]. However, Bhavsar et al. [103] reported the complete degradation of MSN calcined at 540 °C, both *in vitro* and *in vivo* studies in less than a week. On the other hand, dialysed MSN present very low consolidation, similar to extracted ones, which leads to a high degradability [44,98].

In this context, we studied the degradability of the nanoparticles **MSN-400**, **MSN-500**, **MSN-550,** and **MSN-extHCl**. For this purpose, samples of these solids were suspended in PBS at pH 7.4, to simulate physiological conditions, at a concentration of 1 mg/ml. The solids were stirred for two weeks at room temperature, and aliquots were taken at different times (0, 1, 4, 7, and 14 days) and characterised by TEM, PXRD, and DLS. TEM images are shown in Fig. 7 (additional images are shown in Supplementary Information, Fig. S1). All samples show evidence of progressive degradation over time. On the one hand, the degradation was more noticeable for solids that were obtained at lower calcination temperatures. Thus **MSN-400** shows the highest level of degradation among the calcined samples. In contrast, **MSN-550** shows high stability and low degradation over the recorded time. Besides, the extracted sample **MSN-extHCl** shows even greater signs of degradation than **MSN-400**.

As a consequence of degradation, several processes were observed. First, the surface of the nanoparticles becomes very rough even at the initial stages. This is provoked by the hydrolysis of silica starting at the surface and progressing towards the centre of the nanoparticle [97]. Consequently, a decrease in the size of the nanoparticles was observed for all samples, even after the first day of assay. Fig. S2 collects the evolution with time of the average sizes of the studied samples, calculated using TEM measurements. In fact, the size of the nanoparticles tends to shrink more rapidly in the first few days and more slowly thereafter. This behaviour is compatible with that described by He et al. [96] and other authors [102], who also reported that the degradation was faster during the first hours but then stabilised. The downsizing in **MSN-550** nanoparticles (from 89 nm to ca. 71 nm after 14 days) is lower than for the other samples. In the case of **MSN-500**, the decrease in the size of the nanoparticles is slightly higher, reaching 66 nm after 14 days. In the case of **MSN-400** and **MSN-extHCl,** further size reduction was observed, but the formation of an amorphous and aggregated mass after 1 and 4 days, respectively, makes it difficult to distinguish individual nanoparticles and thus measure their size.

Table 4
Nanoparticles appearance as a function of the soaking time for samples obtained with different method for the removal of the surfactant.

SAMPLE	MSN-400	MSN-500	MSN-550	MSN-ExtHCl
Day 0	++	++	++	++
Day 1	++	++	++	+
Day 4	+	+	++	–
Day 7	–	+	++	–
Day 14	–	+	+	–

- Highly aggregated MSN, formation of amorphous mass, difficult to distinguish them.
++Mostly spherical-shaped MSN, surfaces distinguishable from each other.
+Mostly spherical-shaped and highly fused MSN, surfaces not clearly distinguishable from each other.

Size evolution was also monitored by DLS (Fig. S3). In this case, the data obtained did not show a decrease in the mean particle size over time, but rather an increase and, more importantly, a broadening of the size distribution curves. This effect has also been observed in other studies [35] and has been hypothesised to be related to an increase in the fusion between the nanoparticles as the degradation process progresses. In this context, the samples **MSN-550** and **MSN-500** showed fewer changes over time in their DLS curves and less aggregate formation. In contrast, **MSN-400** and **MSN-extHCl** showed a shift of their size distribution towards larger sizes, due to the formation of a high number of fused clusters of nanoparticles, which were also observed in the TEM images, especially for the **MSN-extHCl** material.

Regarding the degradation phenomena, Table 4 summarises the qualitative state of each MSN sample over time according to the appearance of the nanoparticles, namely, the shape regularity, the

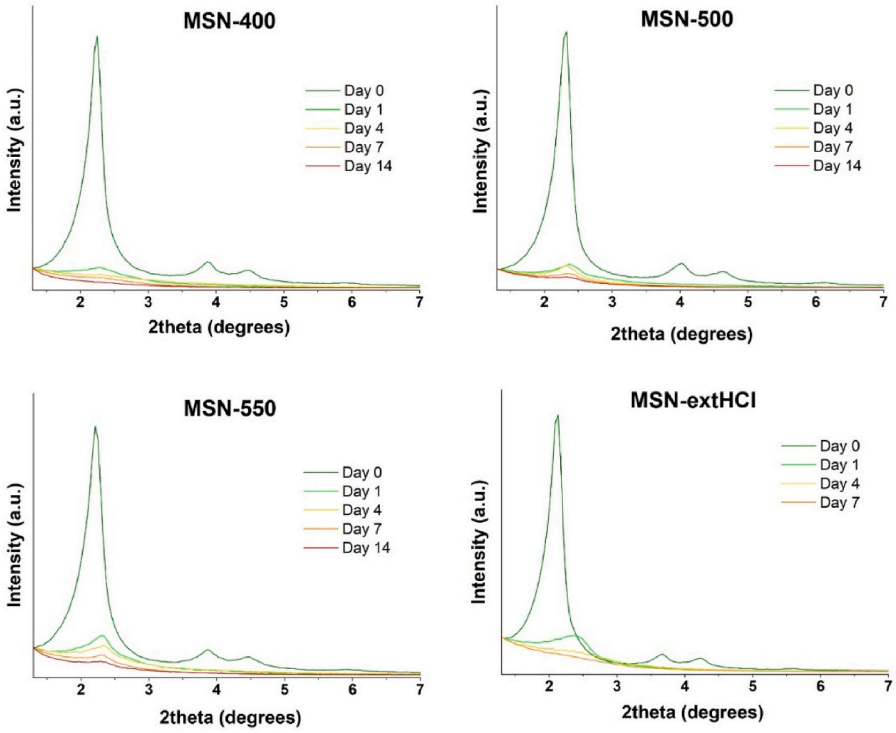

Fig. 8. Biodegradability assay. PXRD patterns of calcined and extracted samples over time (0, 1, 4, 7, and 14 days). The PXRD pattern of MSN-extHCl at 14 days was not measured as after 7 days no signal was found.

maintenance of the silica mesostructured silica network and the formation of fusions between nanoparticles.

Another visible phenomenon associated with the degradation of the nanoparticles was the loss of order in the mesoporosity, which has been widely reported [90,102]. Changes in the mesoporosity were determined based on the analysis of the PXRD diagrams (Fig. 8) and the careful observation of the TEM images (Fig. 7). The diffraction patterns show a generalized and progressive loss of crystallinity in all the samples. Particularly, while the main (100) peak suffers a progressive intensity decrease and width increase, the peaks (110), (200) and (210) disappear from the pattern of the samples already after the first day of treatment. This general change is faster in the case of MSN-extHCl and MSN-400. TEM images also show that the ratio of nanoparticles which possess visible and ordered mesoporosity (parallel channels or hexagonally arranged pores) decreases over time in all the samples, following the same trend that the one observed in PRXD (**MSN-extHCl** > **MSN-400** > **MSN-500** > **MSN-550**). Therefore, the robustness of the mesostructure against degradation followed the same trend observed throughout the study, namely, the higher the calcination temperature, the greater the robustness of the structure and the lower ease of degradation.

According to the results obtained, it can be said that both the calcined and the extracted samples showed evidence of degradation under the conditions used. Furthermore, it has been shown that the rate of degradation is higher when the condensation degree of the silica framework is smaller. Thus, **MSN-400** and **MSN-ExtHCl** show a high level of degradation while **MSN-500** and **MSN-550** maintain the ordered mesoporosity for a longer time. Therefore, the rate of degradation is correlated with the surfactant removal method and, for the calcined samples, with the temperature of calcination. Furthermore, the degradation process is associated with several effects on the nanoparticles: 1) the surface of the nanoparticles becomes rough; 2) the size of the nanoparticles decreases with days, especially at the beginning; 3) nanoparticles fuse with each other and form aggregated clusters; 4) amorphous silica agglomerates appear and the ordered mesoporosity of remaining nanoparticles decreases. The fusions, the loss of mesoporosity and the precipitation of amorphous silica are caused because the hydrolysis process is accompanied by condensation reactions that in the absence of the template produce the breakdown of the mesoporous structure [104].

4. Conclusions

In this work, we present a systematic study of the implications of the surfactant removal method in MCM-41-type MSN. Different calcined and extracted samples are compared, using calcination at different temperatures (400, 450, 500 and 550 °C) and two different surfactant extraction methods (HCl-ethanol and NH_4NO_3-ethanol). The study encompasses the analysis of the surfactant removal efficiency, the silica condensation degree, the silica network and mesoporosity, the cytotoxicity, and the biodegradation rate. This methodological approach provides a new comprehensive perspective of the implications of the use of the different methods for removing the surfactant on the characteristics of the nanoparticles, especially for biomedical applications. Furthermore, it also provides a deeper knowledge about the surfactant removal process itself. We remark the importance of this study taking into account the discrepancies we found in the literature about this matter. The information this study provides will help to select the surfactant removal method and tune the specific condition to obtain nanomaterials with desired properties. For example, on account of the performed studies with MCM-41-type MSN, we can suggest that the calcination below 500 °C should be avoided as coke residues remains in the nanoparticles. Additionally, the use of calcination method at 500 °C or the use of extracted MSN can be better than the standard calcination at 550 °C in terms of rapid biodegradability, such as some biomedical applications which need a rapid degradation (drug or gene delivery, short-term medical imaging or sensing). Nevertheless, if the application of MSN requires long-term use, such as in the case of catalysis, adsorption and some long-term biomedical applications (tissue engineering, long-term medical imaging, etc.), higher calcination temperatures can

be more suitable considering the longer lifetime that confers a higher silica condensation degree. Finally, if solvent extraction method is used, it must be taken into account the presence of ethoxy groups for the properties of the nanoparticles.

CRediT authorship contribution statement

Vicente Candela-Noguera: Writing – original draft, Investigation, Conceptualization. **Pedro Amorós:** Investigation, Formal analysis. **Elena Aznar:** Supervision, Funding acquisition. **María Dolores Marcos:** Conceptualization, Funding acquisition, Supervision, Writing – review & editing. **Ramón Martínez-Máñez:** Conceptualization, Funding acquisition, Writing – review & editing.

Declaration of competing interest

The authors declare that they have no known competing financial interests or personal relationships that could have appeared to influence the work reported in this paper.

Data availability

Data will be made available on request.

Acknowledgements

V.C.-N. thanks the Spanish Government for his fellowship (FPU15/02753). This research was supported by projects PID2021-126304OB-C41, PID2021-126304OB-C43 and PID2021-128141OB-C22 funded by MCIN/AEI/10.13039/501100011033/and by European Regional Development Fund - A way of doing Europe. This study also forms part of the Advanced Materials programme (MFA/2022/049 and MFA/2022/053) and was supported by MCIN with funding from European Union NextGenerationEU (PRTR-C17.I1) and by Generalitat Valenciana. This study was also supported by Generalitat Valenciana (CIPROM/2021/007). This research was also supported by CIBER -Consorcio Centro de Investigación Biomédica en Red- (CB07/01/2012), Instituto de Salud Carlos III, Ministerio de Ciencia e Innovación. The authors also thank the Electron Microscopy Service at UPV and SCSIE at UV for support. NMR was registered at the U26 facility of ICTS "NANBIOSIS" at the Universitat of València.

Appendix A. Supplementary data

Supplementary data to this article can be found online at https://doi.org/10.1016/j.micromeso.2024.113119.

References

[1] M. Manzano, M. Vallet-Regí, Mesoporous silica nanoparticles in nanomedicine applications, J. Mater. Sci. Mater. Med. 29 (2018) 65, https://doi.org/10.1007/s10856-018-6069-x.
[2] B. Xu, S. Li, R. Shi, H. Liu, Multifunctional mesoporous silica nanoparticles for biomedical applications, Signal Transduct. Targeted Ther. 8 (2023) 435, https://doi.org/10.1038/s41392-023-01654-7.
[3] A. García-Fernández, E. Aznar, R. Martínez-Máñez, F. Sancenón, New advances in in vivo applications of gated mesoporous silica as drug delivery nanocarriers, Small 16 (2020) 1902242, https://doi.org/10.1002/smll.201902242.
[4] I. Garrido-Cano, A. Adam-Artigues, A. Lameirinhas, J.F. Blandez, V. Candela-Noguera, F. Rojo, S. Zazo, J. Madoz-Gúrpide, A. Lluch, B. Bermejo, F. Sancenón, J.M. Cejalvo, R. Martínez-Máñez, P. Eroles, miR-99a-5p modulates doxorubicin resistance via the COX-2/ABCG2 axis in triple-negative breast cancer: from the discovery to in vivo studies, Cancer Commun. 42 (2022) 1412–1416, https://doi.org/10.1002/cac2.12352.
[5] A. Llopis-Lorente, P. Díez, A. Sánchez, M.D. Marcos, F. Sancenón, P. Martínez-Ruiz, R. Villalonga, R. Martínez-Máñez, Interactive models of communication at the nanoscale using nanoparticles that talk to one another, Nat. Commun. 8 (2017) 15511, https://doi.org/10.1038/ncomms15511.
[6] B. de Luis, A. Llopis-Lorente, F. Sancenón, R. Martínez-Máñez, Engineering chemical communication between micro/nanosystems, Chem. Soc. Rev. 50 (2021) 8829–8856, https://doi.org/10.1039/D0CS01048K.
[7] P. Díez, E. Lucena-Sánchez, A. Escudero, A. Llopis-Lorente, R. Villalonga, R. Martínez-Máñez, Ultrafast directional janus Pt-mesoporous silica nanomotors for smart drug delivery, ACS Nano 15 (2021) 4467–4480, https://doi.org/10.1021/acsnano.0c08404.
[8] P.L. Venugopalan, B. Esteban-Fernández De Ávila, M. Pal, A. Ghosh, J. Wang, Fantastic voyage of nanomotors into the cell, ACS Nano 14 (2020) 9423–9439, https://doi.org/10.1021/acsnano.0c05217.
[9] F. Sancenón, L. Pascual, M. Oroval, E. Aznar, R. Martínez-Máñez, Gated silica mesoporous materials in sensing applications, ChemistryOpen 4 (2015) 418–437, https://doi.org/10.1002/open.201500053.
[10] M. Parra, S. Gil, P. Gaviña, A.M. Costero, Mesoporous silica nanoparticles in chemical detection: from small species to large bio-molecules, Sensors 22 (2021) 261, https://doi.org/10.3390/s22010261.
[11] A. Bernardos, E. Piacenza, F. Sancenón, M. Hamidi, A. Maleki, R.J. Turner, R. Martínez-Máñez, Mesoporous silica-based materials with bactericidal properties, Small 15 (2019) 1900669, https://doi.org/10.1002/smll.201900669.
[12] D.C. Yu Lai, Mesoporous silica nanomaterials applications in catalysis, J. Thermodyn. Catal. 5 (2014) 10–12, https://doi.org/10.4172/2157-7544.1000e124.
[13] R.E. Morris, P.S. Wheatley, Gas storage in nanoporous materials, Angew. Chem. Int. Ed. 47 (2008) 4966–4981, https://doi.org/10.1002/anie.200703934.
[14] A. Yildirim, M. Turkaydin, B. Garipcan, M. Bayindir, Cytotoxicity of multifunctional surfactant containing capped mesoporous silica nanoparticles, RSC Adv. 6 (2016) 32060–32069, https://doi.org/10.1039/C5RA21722A.
[15] Q. He, Z. Zhang, Y. Gao, J. Shi, Y. Li, Intracellular localization and cytotoxicity of spherical mesoporous silica Nano- and microparticles, Small 5 (2009) 2722–2729, https://doi.org/10.1002/smll.200900923.
[16] S.P. Hudson, R.F. Padera, R. Langer, D.S. Kohane, The biocompatibility of mesoporous silicates, Biomaterials 29 (2008) 4045–4055, https://doi.org/10.1016/j.biomaterials.2008.07.007.
[17] M. Barczak, Template removal from mesoporous silicas using different methods as a tool for adjusting their properties, New J. Chem. 42 (2018) 4182–4191, https://doi.org/10.1039/C7NJ04642A.
[18] A.M. Basso, B.P. Nicola, K. Bernardo-Gusmão, S.B.C. Pergher, Tunable effect of the calcination of the silanol groups of KIT-6 and SBA-15 mesoporous materials, Appl. Sci. 10 (2020) 1–16, https://doi.org/10.3390/app10030970.
[19] T. Asefa, Z. Tao, Biocompatibility of mesoporous silica nanoparticles, Chem. Res. Toxicol. 25 (2012) 2265–2284, https://doi.org/10.1021/tx300166u.
[20] V. Cauda, C. Argyo, D.G. Piercey, T. Bein, "Liquid-phase calcination" of colloidal mesoporous silica nanoparticles in high-boiling solvents, J. Am. Chem. Soc. 133 (2011) 6484–6486, https://doi.org/10.1021/ja1067492.
[21] F. Lu, S.H. Wu, Y. Hung, C.Y. Mou, Size effect on cell uptake in well-suspended, uniform mesoporous silica nanoparticles, Small 5 (2009) 1408–1413, https://doi.org/10.1002/smll.200900005.
[22] S.H. Wu, H.P. Lin, Synthesis of mesoporous silica nanoparticles, Chem. Soc. Rev. 42 (2013) 3862–3875, https://doi.org/10.1039/c3cs35405a.
[23] M. Barczak, Template removal from mesoporous silicas using different methods as a tool for adjusting their properties, New J. Chem. 42 (2018) 4182–4191, https://doi.org/10.1039/c7nj04642a.
[24] L. Mahoney, R.T. Koodali, Versatility of Evaporation-Induced Self-Assembly (EISA) method for preparation of mesoporous TiO2 for energy and environmental applications, Materials 7 (2014) 2697–2746, https://doi.org/10.3390/ma7042697.
[25] I. Mukherjee, A. Mylonakis, Y. Guo, S.P. Samuel, S. Li, R.Y. Wei, A. Kojtari, Y. Wei, Effect of nonsurfactant template content on the particle size and surface area of monodisperse mesoporous silica nanospheres, Microporous Mesoporous Mater. 122 (2009) 168–174, https://doi.org/10.1016/j.micromeso.2009.02.030.
[26] Q. Cai, Z.S. Luo, W.Q. Pang, Y.W. Fan, X.H. Chen, F.Z. Cui, Dilute solution routes to various controllable morphologies of MCM-41 silica with a basic medium, Chem. Mater. 13 (2001) 258–263, https://doi.org/10.1021/cm990661z.
[27] S. Bhattacharyya, G. Lelong, M.L. Saboungi, Recent progress in the synthesis and selected applications of MCM-41: a short review, J. Exp. Nanosci. 1 (2006) 375–395, https://doi.org/10.1080/17458080600812757.
[28] R. Kumar, H.T. Chen, J.L.V. Escoto, V.S.Y. Lin, M. Pruski, Template removal and thermal stability of organically functionalized mesoporous silica nanoparticles, Chem. Mater. 18 (2006) 4319–4327, https://doi.org/10.1021/cm060598v.
[29] J. Kecht, T. Bein, Functionalization of colloidal mesoporous silica by metalorganic reagents, Langmuir 24 (2008) 14209–14214, https://doi.org/10.1021/la802115n.
[30] T. Aumond, L. Pinard, C. Batiot-Dupeyrat, A. Sachse, Non-thermal plasma: a fast and efficient template removal approach allowing for new insights to the SBA-15 structure, Microporous Mesoporous Mater. 296 (2020) 110015, https://doi.org/10.1016/j.micromeso.2020.110015.
[31] E.W.S.J.C. Vartuli, K.D. Schmitt, C.T. Kresge, W.J. Roth, M.E. Leonowicz, S. B. McCullen, S.D. Hellring, J.S. Beck, J.L. Schlenker, D.H. Olson, Effect of surfactant/silica molar ratios on the formation of mesoporous molecular sieves : inorganic, Chem. Mater. 6 (1994) 2317–2326, https://doi.org/10.1021/cm00048a018.
[32] Z. Zhang, A. Mayoral, I. Melián-Cabrera, Protocol optimization for the mild detemplation of mesoporous silica nanoparticles resulting in enhanced texture and colloidal stability, Microporous Mesoporous Mater. 220 (2016) 110–119, https://doi.org/10.1016/j.micromeso.2015.08.026.
[33] C. Sanfeliu, R. Martínez-Máñez, F. Sancenón, J. Soto, P. Amorós, T. Azaïs, M. D. Marcos, 11B-MAS NMR approach to the boron adsorption mechanism on a glucose-functionalised mesoporous silica matrix, Microporous Mesoporous Mater. 266 (2018) 232–241, https://doi.org/10.1016/j.micromeso.2018.02.016.

[34] K.M.L. Taylor, J.S. Kim, W.J. Rieter, H. An, W. Lin, W. Lin, Mesoporous silica nanospheres as highly efficient MRI contrast agents, J. Am. Chem. Soc. 130 (2008) 2154–2155, https://doi.org/10.1021/ja710193c.
[35] L. Yu, Y. Chen, M. Wu, X. Cai, H. Yao, L. Zhang, H. Chen, J. Shi, Manganese extraction" strategy enables tumor-sensitive biodegradability and theranostics of nanoparticles, J. Am. Chem. Soc. 138 (2016) 9881–9894, https://doi.org/10.1021/jacs.6b04299.
[36] N. Lang, A. Tuel, A fast and efficient ion-exchange procedure to remove surfactant molecules from MCM-41 materials, Chem. Mater. 16 (2004) 1961–1966, https://doi.org/10.1021/cm030633n.
[37] A. Hernández Montoto, R. Montes, A. Samadi, M. Gorbe, J.M. Terrés, R. Cao-Milán, E. Aznar, J. Ibañez, R. Masot, M.D. Marcos, M. Orzáez, F. Sancenón, L. B. Oddershede, R. Martínez-Máñez, Gold nanostars coated with mesoporous silica are effective and nontoxic photothermal agents capable of gate keeping and laser-induced drug release, ACS Appl. Mater. Interfaces 10 (2018) 27644–27656, https://doi.org/10.1021/acsami.8b08395.
[38] Q. He, J. Shi, F. Chen, M. Zhu, L. Zhang, An anticancer drug delivery system based on surfactant-templated mesoporous silica nanoparticles, Biomaterials 31 (2010) 3335–3346, https://doi.org/10.1016/j.biomaterials.2010.01.015.
[39] J. Feng, Z. Wang, B. Shen, L. Zhang, X. Yang, N. He, Effects of template removal on both morphology of mesoporous silica-coated gold nanorod and its biomedical application, RSC Adv. 4 (2014) 28683–28690, https://doi.org/10.1039/C4RA03122A.
[40] M.S. Kim, J.Y. Chang, Preparation of multifunctional mesoporous silica particles: the use of an amphiphilic silica precursor with latent amine functionality in selective functionalization of the inner surface, J. Mater. Chem. 21 (2011) 8766, https://doi.org/10.1039/c1jm10440c.
[41] M. Varache, I. Bezverkhyy, L. Saviot, F. Bouyer, F. Baras, F. Bouyer, Optimization of MCM-41 type silica nanoparticles for biological applications: control of size and absence of aggregation and cell cytotoxicity, J. Non-Cryst. Solids 408 (2015) 87–97, https://doi.org/10.1016/j.jnoncrysol.2014.10.020.
[42] K. Möller, J. Kobler, T. Bein, Colloidal suspensions of nanometer-sized mesoporous silica, Adv. Funct. Mater. 17 (2007) 605–612, https://doi.org/10.1002/adfm.200600578.
[43] B.Y. Hung, Y. Kuthati, R.K. Kankala, S. Kankala, J.P. Deng, C.L. Liu, C.H. Lee, Utilization of enzyme-immobilized mesoporous silica nanocontainers (IBN-4) in prodrug-activated cancer theranostics, Nanomaterials 5 (2015) 2169–2191, https://doi.org/10.3390/nano5042169.
[44] H. Yamada, C. Urata, Y. Aoyama, S. Osada, Y. Yamauchi, K. Kuroda, Preparation of colloidal mesoporous silica nanoparticles with different diameters and their unique degradation behavior in static aqueous systems, Chem. Mater. 24 (2012) 1462–1471, https://doi.org/10.1021/cm3001688.
[45] A. da C. Schneid, C.P. Silveira, F.E. Galdino, L.F. Ferreira, K. Bouchmella, M. B. Cardoso, Colloidal stability and redispersibility of mesoporous silica nanoparticles in biological media, Langmuir 36 (2020) 11442–11449, https://doi.org/10.1021/acs.langmuir.0c01571.
[46] L.S. Wang, L.C. Wu, S.Y. Lu, L.L. Chang, I.T. Teng, C.M. Yang, J.A.A. Ho, Biofunctionalized phospholipid-capped mesoporous silica nanoshuttles for targeted drug delivery: improved water suspensibility and decreased nonspecific protein binding, ACS Nano 4 (2010) 4371–4379, https://doi.org/10.1021/nn901376h.
[47] H. Yamada, H. Ujiie, C. Urata, E. Yamamoto, Y. Yamauchi, K. Kuroda, A multifunctional role of trialkylbenzenes for the preparation of aqueous colloidal mesostructured/mesoporous silica nanoparticles with controlled pore size, particle diameter, and morphology, Nanoscale 7 (2015) 19557–19567, https://doi.org/10.1039/C5NR04465K.
[48] E. Yamamoto, M. Kitahara, T. Tsumura, K. Kuroda, Preparation of size-controlled monodisperse colloidal mesoporous silica nanoparticles and fabrication of colloidal crystals, Chem. Mater. 26 (2014) 2927–2933, https://doi.org/10.1021/cm500619p.
[49] C. Urata, Y. Aoyama, A. Tonegawa, Y. Yamauchi, K. Kuroda, Dialysis process for the removal of surfactants to form colloidal mesoporous silica nanoparticles, Chem. Commun. (2009) 5094–5096, https://doi.org/10.1039/b908625k.
[50] Z. Zhang, I. Melián-Cabrera, Modifying the hierarchical porosity of SBA-15 via mild-detemplation followed by secondary treatments, J. Phys. Chem. C 118 (2014) 28689–28698, https://doi.org/10.1021/jp5096213.
[51] Z. Kheshti, S. Hassanajili, Surfactant Removal from Mesoporous Silica Shell of Core-Shell Magnetic Microspheres by, 2017.
[52] Y. Liu, Y. Pan, Z.J. Wang, P. Kuai, C.J. Liu, Facile and fast template removal from mesoporous MCM-41 molecular sieve using dielectric-barrier discharge plasma, Catal. Commun. 11 (2010) 551–554, https://doi.org/10.1016/j.catcom.2009.12.017.
[53] H. Ghaedi, M. Zhao, Review on template removal techniques for synthesis of mesoporous silica materials, Energy Fuel. 36 (2022) 2424–2446, https://doi.org/10.1021/acs.energyfuels.1c04435.
[54] N. Zainuddin, I. Ahmad, H. Kargarzadeh, S. Ramli, Hydrophobic kenaf nanocrystalline cellulose for the binding of curcumin, Carbohydr. Polym. 163 (2017) 261–269, https://doi.org/10.1016/j.carbpol.2017.01.036.
[55] H. Yan, X. hu Zhang, J. ming Wu, L. qiao Wei, X. guang Liu, B. she Xu, The use of CTAB to improve the crystallinity and dispersibility of ultrafine magnesium hydroxide by hydrothermal route, Powder Technol. 188 (2008) 128–132, https://doi.org/10.1016/j.powtec.2008.04.024.
[56] S. Hosseini, A.B. Mohamad, A.H. KaHum, W.R. Wan Daud, Thermal analysis of CsH2PO4 nanoparticles using surfactants CTAB and F-68, in: J. Therm. Anal. Calorim., Springer, 2010, pp. 197–202, https://doi.org/10.1007/s10973-009-0132-2.
[57] A.M. Alswieleh, A.M. Beagan, B.M. Alsheheri, K.M. Alotaibi, M.D. Alharthi, M. S. Almeataq, Hybrid mesoporous silica nanoparticles grafted with 2-(tert-butylamino)ethyl methacrylate-b-poly(ethylene glycol) methyl ether methacrylate diblock brushes as drug nanocarrier, Molecules 25 (2020) 195, https://doi.org/10.3390/molecules25010195.
[58] G.E. Musso, E. Bottinelli, L. Celi, G. Magnacca, G. Berlier, Influence of surface functionalization on the hydrophilic character of mesoporous silica nanoparticles, Phys. Chem. Chem. Phys. 17 (2015) 13882–13894, https://doi.org/10.1039/C5CP00552C.
[59] J. Kobler, K. Möller, T. Bein, Colloidal suspensions of functionalized mesoporous silica nanoparticles, ACS Nano 2 (2008) 791–799, https://doi.org/10.1021/nn700008s.
[60] U. Nithiyanantham, S.R. Ede, M.F. Ozaydin, H. Liang, A. Rathishkumar, S. Kundu, Low temperature, shape-selective formation of Sb2Te3 nanomaterials and their thermoelectric applications, RSC Adv. 5 (2015) 89621–89634, https://doi.org/10.1039/c5ra17284e.
[61] M. Bera, Chandravati, P. Gupta, P.K. Maji, Facile one-pot synthesis of graphene oxide by sonication assisted mechanochemical approach and its surface chemistry, J. Nanosci. Nanotechnol. 18 (2018) 902–912, https://doi.org/10.1166/JNN.2018.14306.
[62] B. Kartick, S.K. Srivastava, I. Srivastava, Green synthesis of graphene, J. Nanosci. Nanotechnol. 13 (2013) 4320–4324, https://doi.org/10.1166/JNN.2013.7461.
[63] C.Y. Chen, H.X. Li, M.E. Davis, Studies on mesoporous materials. I. Synthesis and characterization of MCM-41, Microporous Mater. 2 (1993) 17–26, https://doi.org/10.1016/0927-6513(93)80058-3.
[64] F. Kleitz, W. Schmidt, F. Schüth, Calcination behavior of different surfactant-templated mesostructured silica materials, Microporous Mesoporous Mater. 65 (2003) 1–29, https://doi.org/10.1016/S1387-1811(03)00506-7.
[65] T. Peng, D. Zhao, K. Dai, W. Shi, K. Hirao, Synthesis of titanium dioxide nanoparticles with mesoporous anatase wall and high photocatalytic activity, J. Phys. Chem. B 109 (2005) 4947–4952, https://doi.org/10.1021/jp044771r.
[66] G.J.A.A. Soler-Illia, A. Louis, C. Sanchez, Synthesis and characterization of mesostructured titania-based materials through evaporation-induced self-assembly, Chem. Mater. 14 (2002) 750–759, https://doi.org/10.1021/cm011217a.
[67] Y. Ding, C. Zhao, Y. Li, Z. Ma, X. Lv, Effect of calcination temperature on the structure and catalytic performance of the cu-mcm-41 catalysts for the synthesis of dimethyl carbonate, Quim. Nova 41 (2018) 1156–1161, https://doi.org/10.21577/0100-4042.20170291.
[68] V.V. Potapov, L.T. Zhuravlev, Temperature dependence of the concentration of silanol groups in silica precipitated from a hydrothermal solution, Glas, Phys. Chem. 31 (2005) 661–670, https://doi.org/10.1007/s10720-005-0111-z.
[69] J. Goworek, A. Kierys, W. Gac, A. Borówka, R. Kusak, Thermal degradation of CTAB in as-synthesized MCM-41, J. Therm. Anal. Calorim. 96 (2009) 375–382, https://doi.org/10.1007/s10973-008-9055-6.
[70] R. Saha, R.V.S. Uppaluri, P. Tiwari, Effects of interfacial tension, oil layer break time, emulsification and wettability alteration on oil recovery for carbonate reservoirs, Colloids Surfaces A Physicochem. Eng. Asp. 559 (2018) 92–103, https://doi.org/10.1016/j.colsurfa.2018.09.045.
[71] S. Li, S. Yang, S. Xu, Q. Wan, Influence of heat treatment on the microstructure and surface groups of Stöber silica, Mater. Res. Express 10 (2023) 105004, https://doi.org/10.1088/2053-1591/acff3e.
[72] T. Kimura, K. Kuroda, Y. Sugahara, Esterification of the silanol groups in the mesoporous silica derived from kanemite, J. Porous Mater. 5 (1998) 127–132.
[73] D. Tarn, C.E. Ashley, M. Xue, E.C. Carnes, J.I. Zink, C.J. Brinker, Mesoporous silica nanoparticle nanocarriers: biofunctionality and biocompatibility, Acc. Chem. Res. 46 (2013) 792–801, https://doi.org/10.1021/ar3000986.
[74] Y.-S. Lin, C.L. Haynes, Impacts of mesoporous silica nanoparticle size, pore ordering, and pore integrity on hemolytic activity, J. Am. Chem. Soc. 132 (2010) 4834–4842, https://doi.org/10.1021/ja910846q.
[75] P. Riachy, F. Roig, M.-J. García-Celma, M.-J. Stébé, A. Pasc, J. Esquena, C. Solans, J.L. Blin, Hybrid hierarchical porous silica templated in nanoemulsions for drug release, Eur. J. Inorg. Chem. 2016 (2016) 1989–1997, https://doi.org/10.1002/ejic.201501127.
[76] S.C. Feifel, F. Lisdat, Silica nanoparticles for the layer-by-layer assembly of fully electro-active cytochrome c multilayers, J. Nanobiotechnol. 9 (2011) 59, https://doi.org/10.1186/1477-3155-9-59.
[77] S.B. McCullen, J.C. Vartuli, C.T. Kresge, W.J. Roth, J.S. Beck, K.D. Schmitt, M. E. Leonowicz, J.L. Schlenker, S.S. Shih, J.D. Lutner, A new family of mesoporous molecular sieves, in: Access Nanoporous Mater, 2006, pp. 1–11, https://doi.org/10.1007/0-306-47066-7_1.
[78] K.W. Gallis, C.C. Landry, Synthesis of MCM-48 by a phase transformation process, Chem. Mater. 9 (1997) 2035–2038, https://doi.org/10.1021/cm970482m.
[79] Q. Huo, D.I. Margolese, U. Ciesla, D.G. Demuth, P. Feng, T.E. Gier, P. Sieger, A. Firouzi, B.F. Chmelka, F. Schuth, G.D. Stucky, Organization of organic molecules with inorganic molecular species into nanocomposite biphase arrays, Chem. Mater. 6 (1994) 1176–1191, https://doi.org/10.1021/cm00044a016.
[80] A. Stein, B.J. Melde, R.C. Schroden, Hybrid inorganic-organic mesoporous silicates-nanoscopic reactors coming of age, Adv. Mater. 12 (2000) 1403–1419, https://doi.org/10.1002/1521-4095(200010)12:19<1403::AID-ADMA1403>3.0.CO;2-X.
[81] V. Candela-Noguera, M. Alfonso, P. Amorós, E. Aznar, M.D. Marcos, R. Martínez-Máñez, In-depth study of factors affecting the formation of MCM-41-type mesoporous silica nanoparticles, Microporous Mesoporous Mater. 363 (2024) 112840, https://doi.org/10.1016/j.micromeso.2023.112840.

[82] H.B.S. Chan, P.M. Budd, T.V. De Naylor, Control of mesostructured silica particle morphology, J. Mater. Chem. 11 (2001) 951–957, https://doi.org/10.1039/b005713o.
[83] A. Lérida-Viso, A. Estepa-Fernández, A. García-Fernández, V. Martí-Centelles, R. Martínez-Máñez, Biosafety of mesoporous silica nanoparticles; towards clinical translation, Adv. Drug Deliv. Rev. 201 (2023), https://doi.org/10.1016/j.addr.2023.115049.
[84] D. Tarn, C.E. Ashley, M. Xue, E.C. Carnes, J.I. Zink, C. Jeffrey Brinker, Mesoporous silica nanoparticle nanocarriers-biofunctionality and biocompatibility, Acc. Chem. Res. 46 (2013) 792–801, https://doi.org/10.1021/ar3000986.
[85] J.G. Croissant, Y. Fatieiev, A. Almalik, N.M. Khashab, Mesoporous silica and organosilica nanoparticles: physical chemistry, biosafety, delivery strategies, and biomedical applications, Adv. Healthcare Mater. 7 (2018) 1–75, https://doi.org/10.1002/adhm.201700831.
[86] K. Möller, T. Bein, Degradable drug carriers: vanishing mesoporous silica nanoparticles, Chem. Mater. 31 (2019) 4364–4378, https://doi.org/10.1021/acs.chemmater.9b00221.
[87] V. Cauda, C. Argyo, D.G. Piercey, T. Bein, "Liquid-phase calcination" of colloidal mesoporous silica nanoparticles in high-boiling solvents, J. Am. Chem. Soc. 133 (2011) 6484–6486, https://doi.org/10.1021/ja1067492.
[88] W. Ratirotjanakul, T. Suteewong, D. Polpanich, P. Tangboriboonrat, Amino acid as a biodegradation accelerator of mesoporous silica nanoparticles, Microporous Mesoporous Mater. 282 (2019) 243–251, https://doi.org/10.1016/j.micromeso.2019.02.033.
[89] M. Varache, I. Bezverkhyy, F. Bouyer, R. Chassagnon, F. Baras, F. Bouyer, Improving structural stability of water-dispersed MCM-41 silica nanoparticles through post-synthesis pH aging process, J. Nanoparticle Res. 17 (2015) 356, https://doi.org/10.1007/s11051-015-3147-6.
[90] Y. Choi, J.E. Lee, J.H. Lee, J.H. Jeong, J. Kim, A biodegradation study of SBA-15 microparticles in simulated body fluid and in vivo, Langmuir 31 (2015) 6457–6462, https://doi.org/10.1021/acs.langmuir.5b01316.
[91] X. Li, F. Gao, Y. Dong, X. Li, Strategies to regulate the degradability of mesoporous silica-based nanoparticles for biomedical applications, Nano 14 (2019) 1–13, https://doi.org/10.1142/S1793292019300081.
[92] T.T. Hoang Thi, V. Du Cao, T.N.Q. Nguyen, D.T. Hoang, V.C. Ngo, D.H. Nguyen, Functionalized mesoporous silica nanoparticles and biomedical applications, Mater. Sci. Eng. C 99 (2019) 631–656, https://doi.org/10.1016/j.msec.2019.01.129.
[93] E.B. Ehlerding, F. Chen, W. Cai, Biodegradable and renal clearable inorganic nanoparticles, Adv. Sci. 3 (2015) 1–8, https://doi.org/10.1002/advs.201500223.
[94] S. Yang, L. Chen, X. Zhou, P. Sun, L. Fu, Y. You, M. Xu, Z. You, G. Kai, C. He, Tumor-targeted biodegradable multifunctional nanoparticles for cancer theranostics, Chem. Eng. J. 378 (2019) 122171, https://doi.org/10.1016/j.cej.2019.122171.
[95] J.G. Croissant, C.J. Brinker, Biodegradable Silica-Based Nanoparticles: Dissolution Kinetics and Selective Bond Cleavage, first ed., Elsevier Inc., 2018 https://doi.org/10.1016/bs.enz.2018.07.008.
[96] Q. He, J. Shi, M. Zhu, Y. Chen, F. Chen, The three-stage in vitro degradation behavior of mesoporous silica in simulated body fluid, Microporous Mesoporous Mater. 131 (2010) 314–320, https://doi.org/10.1016/j.micromeso.2010.01.009.
[97] S. Goel, F. Chen, S. Luan, H.F. Valdovinos, S. Shi, S.A. Graves, F. Ai, T.E. Barnhart, C.P. Theuer, W. Cai, Engineering intrinsically zirconium-89 radiolabeled self-destructing mesoporous silica nanostructures for in vivo biodistribution and tumor targeting studies, Adv. Sci. 3 (2016) 1–11, https://doi.org/10.1002/advs.201600122.
[98] S. Seré, B. De Roo, M. Vervaele, S. Van Gool, S. Jacobs, J.W. Seo, J.P. Locquet, Altering the biodegradation of mesoporous silica nanoparticles by means of experimental parameters and surface functionalization, J. Nanomater. 2018 (2018), https://doi.org/10.1155/2018/7390618.
[99] H. Li, H. Guo, C. Lei, L. Liu, L. Xu, Y. Feng, J. Ke, W. Fang, H. Song, C. Xu, C. Yu, X. Long, Nanotherapy in joints: increasing endogenous hyaluronan production by delivering hyaluronan synthase 2, Adv. Mater. 31 (2019) 1–8, https://doi.org/10.1002/adma.201904535.
[100] X. Du, F. Kleitz, X. Li, H. Huang, X. Zhang, S.Z. Qiao, Disulfide-bridged organosilica frameworks: designed, synthesis, redox-triggered biodegradation, and nanobiomedical applications, Adv. Funct. Mater. 28 (2018), https://doi.org/10.1002/adfm.201707325.
[101] X. Li, L. Zhang, X. Dong, J. Liang, J. Shi, Preparation of mesoporous calcium doped silica spheres with narrow size dispersion and their drug loading and degradation behavior, Microporous Mesoporous Mater. 102 (2007) 151–158, https://doi.org/10.1016/j.micromeso.2006.12.048.
[102] V. Cauda, C. Argyo, T. Bein, Impact of different PEGylation patterns on the long-term bio-stability of colloidal mesoporous silica nanoparticles, J. Mater. Chem. 20 (2010) 8693–8699, https://doi.org/10.1039/c0jm01390k.
[103] D. Bhavsar, V. Patel, K. Sawant, Systemic investigation of in vitro and in vivo safety, toxicity and degradation of mesoporous silica nanoparticles synthesized using commercial sodium silicate, Microporous Mesoporous Mater. 284 (2019) 343–352, https://doi.org/10.1016/j.micromeso.2019.04.050.
[104] L. Yu, Y. Chen, H. Lin, W. Du, H. Chen, J. Shi, Ultrasmall mesoporous organosilica nanoparticles: morphology modulations and redox-responsive biodegradability for tumor-specific drug delivery, Biomaterials 161 (2018) 292–305, https://doi.org/10.1016/j.biomaterials.2018.01.046.